# Experimental and numerical investigation on hollow core photonic crystal fiber based bending sensor

YU ZHENG,[1,2] PERRY PING SHUM,[1,2] SHUHUI LIU,[1,3] BOYAO LI,[2,4] YANG XIANG,[1,2] YIYANG LUO,[1,2,*] YANAN ZHANG,[1,5] WENJUN NI,[1,2] ZHIFANG WU,[6] XUAN QUYEN DINH,[1,2,7] SHUWEN ZENG,[8] JEAN-LOUIS AUGUSTE,[8] AND GEORGES HUMBERT[8]

[1]*CINTRA CNRS/NTU/THALES, UMI 3288, Research Techno Plaza, 50 Nanyang Drive, 637553, Singapore*
[2]*School of Electrical and Electronic Engineering, Nanyang Technological University, 639798, Singapore*
[3]*Hubei Key Laboratory of Optical Information and Pattern Recognition, Wuhan Institute of Technology, Wuhan 430205, China*
[4]*Guangzhou Key Laboratory for Special Fiber Photonic Devices, South China Normal University, Guangzhou 510006, China*
[5]*College of Information Science and Engineering, Northeastern University, Shenyang 110819, China*
[6]*Fujian Key Laboratory of Light Propagation and Transformation, College of Information Science and Engineering, Huaqiao University, Xiamen, 361021, China*
[7]*R&T, Thales Solutions Asia Pte Ltd., Singapore 498788, Singapore*
[8]*XLIM Research Institute, UMR 7252 CNRS/University of Limoges, Limoges, 87060, France*
*luoyy@ntu.edu.sg

**Abstract:** Recent progress in designing optimized microstructured optical fiber spreads an application scenario of optical fiber sensing. Here, we investigate the bending measurement based on a specially designed hollow core photonic crystal fiber (HC-PCF). Numerical simulation indicates that the bending sensitivity is mainly determined by the diameter of the hollow core and also depends on the coupled modes. Experimentally, a direction-independent bending sensor is fabricated by sandwiching a segment of specially designed HC-PCF into two segments of single mode fibers. The bending sensitivity of our device is improved 10 times by increasing the diameter of the hollow core. Bending measurement is validated at two orthogonal planes. The maximum sensitivity up to 2.8 nm/deg is obtained at 14° bending angle. Additionally, a low thermal sensitivity of 2.5 pm/°C is observed from 18°C to 1000°C. The sensor is robust, easy to fabricate and cost effective, which is promising in the field of small-angle bending measurement under a large temperature range.

## 1. Introduction

Optical fiber sensors have attracted widespread attention due to their advantages of compact size, high stability, easy integration, repeatability, remote sensing and electromagnetic immunity [1–7]. Bending sensors have been used in many fields such as mechanical engineering, structural monitoring and astronautics. In the past few years, various specialty optical fibers have been developed for bending measurements such as tapered fibers [8–12], microfibers [13,14], multicore optical fibers (MOFs) [15–18], eccentric core fibers (ECFs) [19–21] and polymer optical fibers (POFs) [22,23]. However, tapered fibers or microfibers with a small size are fragile and easily deteriorate by external air flow or dust. MOFs, ECFs and POFs integrated with Bragg gratings exhibit a high sensitivity to temperature variation (50.1 pm/°C) [23]. Hollow core photonic crystal fiber (HC-PCF) characterized by adjustable mode area and high integration can serve as

an optimal platform for developing bending sensors with a low thermal sensitivity due to the low thermo-optic coefficient of the air core.

Liu *et al.* have developed a bending sensor with a low thermal sensitivity by inserting a piece of HC-PCF into two segments of SMFs [24]. Bending was measured by monitoring the angle between two straight parts of HC-PCF located on both sides of bending area. The interference pattern induced by the multimode interference between $HE_{11}$ and $TE_{01}$ modes would shift when the sandwich-structured sensor was bent. It should be noted that lateral offset splicing was needed for exciting the $TE_{01}$ mode. The bending sensitivity was 0.28 nm/deg at 10° with a low temperature sensitivity of 0.5 pm/°C and high stability. However, compared with the ultrahigh sensitive fiber bending sensor (1.27 nm/deg) based on hexagonal lattice PCF under a small angle range (±2°), the limited sensitivity of this device should be optimized for practical applications on small-angle measurement [25]. The basic principle of HC-PCF bending sensors can be attributed to the stretched and compressed fiber material of the outer side and inner side, respectively. Hereby, the refractive index (RI) of the fiber will decrease at the outer side and increase at the inner side when the fiber is bent to a certain direction [26]. The effective optical paths of the guided modes are governed by the changes of material RI, which results in the shift of the interference pattern. It is of great significance to enhance the sensitivity of bending measurements in terms of the advanced design of HC-PCF [27,28].

In this paper, we theoretically and experimentally demonstrated that the bending sensitivity of our sensor at small bending angle was improved 10 times by increasing the diameter of the hollow core compared with [24]. The optical fiber bending sensor was fabricated by splicing a section of specially designed HC-PCF between two segments of SMFs with central alignment. The relationship of the bending sensitivity and the size of hollow core was simulated. The transmission spectra of the device under different lengths of HC-PCF were measured, which indicated that multimode interference between $HE_{11}$ and $HE_{12}$ modes dominates the sensing mechanism. The bending response of the sensor was investigated from -14° to 14° at two orthogonal planes. Then, this sensor was characterized by a low temperature crosstalk from 18 °C to 1000 °C.

## 2. Theoretical analysis

The scanning electron microscope (SEM) cross-sectional image of the specially developed HC-PCF is illustrated in Fig. 1(a). The fiber is made of pure silica via the stack-and-draw process. It is composed of a large hollow-core of 50 μm diameter surrounded by twelve crown-like air holes with a total diameter of 62.5 μm. This design is chosen for limiting the size of the photonic crystal cladding in order to obtain a fiber diameter (128 μm) compatible with standard single mode fibers in fiber-sensor configurations. The thicknesses of the strut between the hollow-core and crown-like air holes, and the strut between two crown-like air holes are about 230 nm and 560 nm, respectively.

The bending sensitivity of this HC-PCF was analyzed by numerically simulating the effective refractive index (ERI) of the modes propagating in the straight and bending configurations. More precisely, we have restrained our study on the interferences of the fundamental mode ($HE_{11}$) to the first higher order mode $TE_{01}$ and to $HE_{12}$ mode which one is the first higher order mode with the same azimuthal symmetry as $HE_{11}$ mode. The ERI of these modes have been simulated with the finite element method (COMSOL Multiphysics) in the straight configuration. The fiber geometry was imported into the simulation model from the SEM image, and the dispersion of silica material was introduced by its Sellmeier equation. Within the wavelength range from 1350 nm to 1650 nm, these modes were propagated in the hollow-core, as illustrated by the distribution of their Poynting vector in Figs. 1(c)–1(e) and their ERI below unity in Fig. 1(f).

The sensing performances of this sensor (illustrated in Fig. 2(a)) were obtained by calculating the interference of two modes, such as $HE_{11}$ mode with $TE_{01}$ or $HE_{12}$ mode. The intensity at a
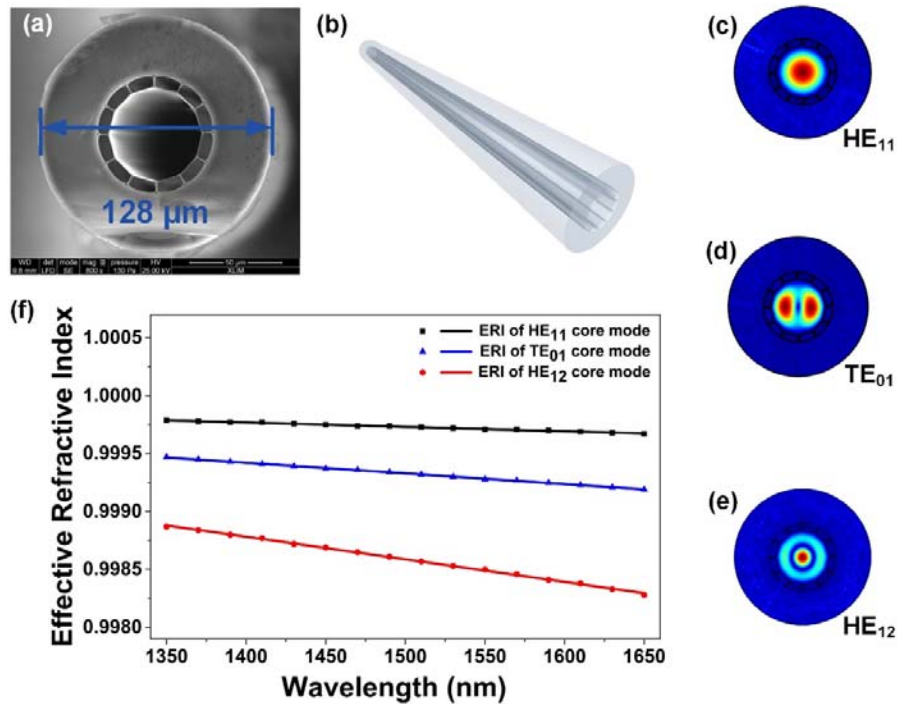
**Fig. 1.** (a) SEM image of the cross section of the HC-PCF; (b) schematic diagram of the HC-PCF; simulated mode distributions of (c) $HE_{11}$ mode, (d) $TE_{01}$ mode and (e) $HE_{12}$ mode at the wavelength of 1550 nm; (f) simulated modal dispersion curves for $HE_{11}$ mode, $TE_{01}$ mode and $HE_{12}$ mode.

given wavelength ($\lambda$) could be calculated with the following equation:

$$I = I_1 + I_2 + 2\sqrt{I_1 I_2} \cos(\Delta\varphi + \varphi_0), \tag{1}$$

$$\Delta\varphi = 2\pi \Delta n_{eff} L / \lambda, \tag{2}$$

where $I_1$ and $I_2$ are the intensities of two interference modes; $\Delta\varphi$ is the phase difference between both modes; $\varphi_0$ is the initial phase difference and $L$ is the length of the HC-PCF for the proposed bending sensor. The transmission spectrum was characterized by typical interference pattern. Transmission reached minimum when $\Delta\varphi + \varphi_0 = (2m + 1)\pi$ (where $m$ is an integer) was fulfilled at specific wavelengths. These wavelength dips were calculated with the following equation:

$$\lambda = 2\pi \Delta n_{eff} L / ((2m + 1)\pi - \varphi_0). \tag{3}$$

The numerical bending sensitivity could be obtained by taking the derivative of Eq. (3) with respect to bending angle ($\theta$):

$$\frac{d\lambda}{d\theta} = \frac{\lambda_0}{\Delta n_0} \frac{d(\Delta n)}{d\theta}, \tag{4}$$

where $\lambda_0 = 2\pi \Delta n_0 L / ((2m + 1)\pi - \varphi_0)$, is the wavelength of a minimum transmission before bending. This equation clearly emphasizes that the bending sensitivity of the sensor is only governed by the variation of the ERI difference ($\Delta n_{eff}$) between two modes.

The variation of ERI versus to the bending angle was simulated by calculating the bending radius associated to the bending angle applied on the fiber. The bending angle was applied on the HC-PCF by keeping one-side straight and forcing the other straight part to be deviated from
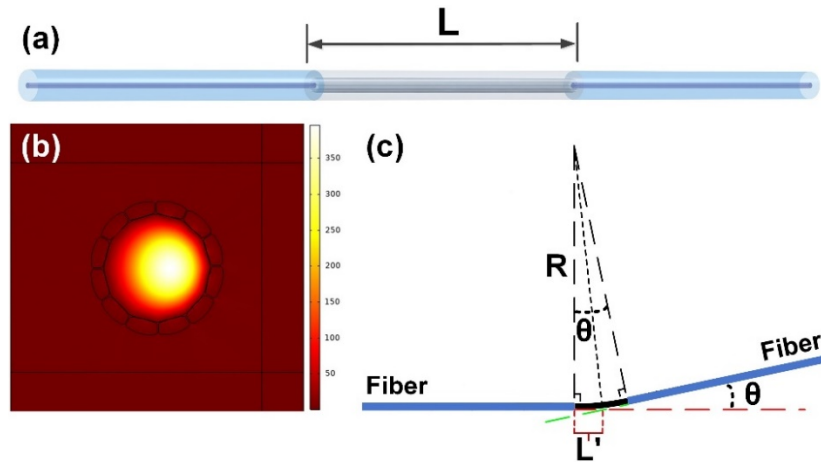
**Fig. 2.** (a) Schematic diagram of the bending sensor; (b) schematic diagram of the simulation model; (c) schematic diagram of the relationship between the bending radius $R$ and the bending angle $\theta$.

the original line (Fig. 2(c)). This deviation defined the bending angle ($\theta$). The bending radius ($R$) was calculated based on the schematic shown in Fig. 2(c). We assumed that the length ($L'$) between the intersection point of two straight lines (two parts of HC-PCF) and the endpoint of bending area was constant, 9 mm. Then the bending radius corresponded to the bending angle based on the triangle:

$$R = L'/tan(\theta/2). \tag{5}$$

For example, for a bending angle $\theta = 2°$, the bending radius was about $R = 515.61$ mm for $L' = 9.00$ mm. The ERI of the modes $HE_{11}$, $TE_{01}$ and $HE_{12}$ were then calculated for different bending angles with the finite element method by applying the process of conformal mapping. The process was to transform the circularly curved fiber into an equivalent straight fiber with modified refractive index distribution. The conformal mapping process is expressed as follows [29–31]:

$$n'(x, y) = (1 + x/R_{eff})n(x, y), \tag{6}$$

where $x$ and $y$ axes are in the local transverse fiber plane; the fiber axis is located at $x = 0$. $R_{eff}$ is the equivalent bending radius; $n(x,y)$ is the refractive index of the straight fiber cross-section. The silica cladding of the fiber was designed as a rectangular surrounded perfectly matched layers for absorbing the radiating modes (Fig. 2(b)). As expected, the mode field distribution shifted away from the core center when the fiber was bent.

We simulated the mode properties of our fabricated HC-PCF (with core diameter of 50 µm) and also for a core diameter of 35 µm similar to the one of the HC-PCF used by Liu *et al.* These simulations would allow us to study the effects of the hollow-core size and the coupled modes on the bending sensitivity and to compare our HC-PCF to the one used by Liu *et al.*

The normalized interference spectra were calculated with the Eqs. (3) and (4), and by applying the assumption of $\varphi_0 = 0$, $I_1 = I_2 = 0.25$ (the input power was equally coupled to both modes). As illustrated in Figs. 3(a)–3(c), the spectra shift to shorter wavelengths with the increase of the bending angle. This shift is not linear and increases with the bending angle. The wavelength shifts of the dip in the interference spectra are plotted in Fig. 3(d) versus the bending angle from 2° to 14°. The bending sensitivity of each wavelength dip is then obtained from the derivative of the wavelength shift (Fig. 3(e)). The shift of the interference spectrum of $HE_{11}$-$TE_{01}$ modes is clearly larger for a hollow-core diameter of 50 µm than of 35 µm (Fig. 3(a) and Fig. 3(b))

with a bending sensitivity slope of 0.168 and 0.024, respectively. For example, this leads to a bending sensitivity improvement of 5 times for bending angle of 10°. The comparison of the interference spectra $HE_{11}$-$TE_{01}$ and $HE_{11}$-$HE_{12}$, for a hollow-core diameter of 50 μm, reveals a higher bending sensitivity of the mode $TE_{01}$ with a slope of 0.168 than the mode $HE_{12}$ (with slope of 0.112), corresponding to bending sensitivity improvement of 1.5 for bending angle of 10°. The comparison of all these simulations demonstrates that the effect of the hollow-core size on the bending sensitivity is larger than the difference between the coupled modes of $HE_{11}$-$TE_{01}$ and $HE_{11}$-$HE_{12}$. These results emphasize the interest of our fiber design that enables the fabrication of large hollow-core for improving the bending sensitivity of the HC-PCF.
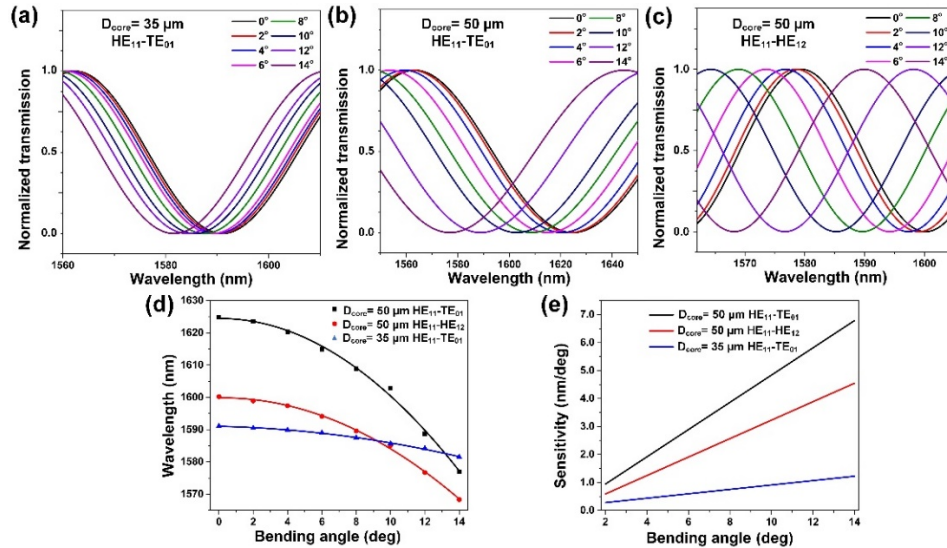


**Fig. 3.** Simulated spectrum of (a) $HE_{11}$-$TE_{01}$ modes of 35-μm-diameter HC-PCF, (b) $HE_{11}$-$TE_{01}$ modes of 50-μm-diameter HC-PCF and (c) $HE_{11}$-$HE_{12}$ modes of 50-μm-diameter HC-PCF; (d) wavelength shift of three kinds of interferences; (e) sensitivity of three kinds of interferences.

## 3. Experimental setup and results

We have fabricated three sensor samples composed of a section of HC-PCF with $L = 1.0$ cm, $L = 2.5$ cm and $L = 5.0$ cm, spliced between two pieces of standard single mode fibers. The samples were spliced by a Fujikura 70S fusion splicer with central alignment. The arc power and arc time were set to -60 bit and 600 ms, respectively, for a robust splicing point without collapse and bubbles. The transmission spectra of these samples plotted in Fig. 4(a) were measured with a broadband light source (Infinon Research 1RBL-11111-F) and an Optical Spectrum Analyzer (OSA, Yokogawa AQ6370c). The free spectral range (FSR) of these spectra are $\Delta\lambda = 175.1$ nm, 60.9 nm, 34.3 nm, respectively for $L = 1.0$ cm, $L = 2.5$ cm and $L = 5.0$ cm. From these values, we can calculate the ERI difference ($\Delta n_{eff}$) with the following equation from [36]:

$$\Delta n_{eff} = \lambda^2/(\Delta\lambda L), \tag{7}$$

with $\lambda$ the central wavelength between two dips. The calculation results of $\Delta n_{eff}$ are all around 1.4 $\times 10^{-3}$. This value is close to the simulated $\Delta n_{eff} = 1.2 \times 10^{-3}$ of the coupling between $HE_{11}$ and $HE_{12}$ modes at 1550 nm (Fig. 1(e)). To confirm this coupling, we have measured the near-field distribution of the light intensity at the output of the 5 cm long length HC-PCF (after cutting

it at the splice point). A tunable laser (Ando AQ4321D) and a camera (Spiricon SP1550M) were used to measure the mode-field distribution at 1541 nm and 1556 nm, respectively in a maximum and a minimum of transmission (as indicated in Fig. 4(a)). The mode distribution at 1541 nm corresponds to the $HE_{11}$ mode (Fig. 4(b)), while the mode distribution at 1556 nm (at a transmission dip) is similar to the one of the $HE_{12}$ mode (Fig. 4(c)). These results reveal that the multimode interferences between $HE_{11}$ and $HE_{12}$ modes dominate the sensing mechanism of our fiber sensor.
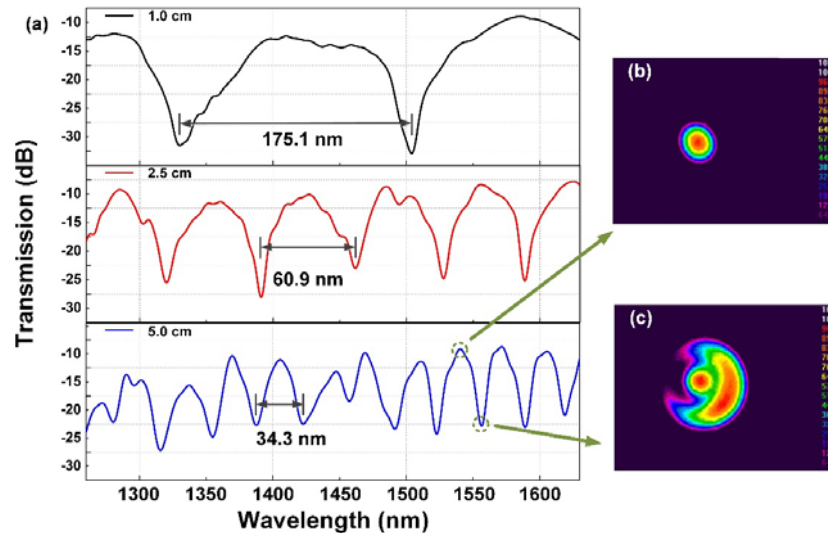


**Fig. 4.** (a) Transmission spectra of the bending sensor with a 1.0 cm, 2.5 cm and 5.0 cm long HC-PCF, respectively; mode field distribution with 5.0 cm long HC-PCF at (b) 1541 nm and (c) 1556 nm, respectively.

The sensor with a 5.0-cm-long length of HC-PCF was used for the bending sensitivity measurements. The HC-PCF was hold in the center on a stage that the position is fixed. The other part (including a portion of the SMF) was filled into a capillary tube. The capillary was attached on a holder that could be moved following a circle arc for applying a bending angle (Fig. 5). The capillary was used for leaving the fiber straight without mechanical strain when it was bent. A protractor ruler was used to measure the bending angle. The different bends were applied with a step of 2°, in the vertical plane ($\alpha$) and then in the horizontal plane ($\beta$), as shown in Fig. 5. The transmission spectrum of the fiber sensor was measured in-line with the broadband light source and the OSA.

As expected from the simulation results (Fig. 3), the transmission spectrum shifted to shorter wavelengths when the bending angle increased, as shown in Fig. 6. The fiber sensor was bent from 0° to both -14° and + 14° in the horizontal plane and then in the vertical plane. Indeed, the measurement range is limited by the special structure of our HC-PCF. Particularly, we can achieve an increased bending sensitivity by using a large hollow core fiber. On the other hand, the large hollow core fiber may be fragile with an increasing bending angle. Hence, there is a tradeoff between the bending sensitivity and the measurement dynamic range. For practical applications, we can optimize our fiber design to satisfy different requirements of the bending measurements. The wavelength of a dip was measured and plotted for each bending angle in the Fig. 7(a). For each bending angle, the position of the dip wavelength was almost identical in both orthogonal planes and also in both opposite directions. These results revealed the direction-independent
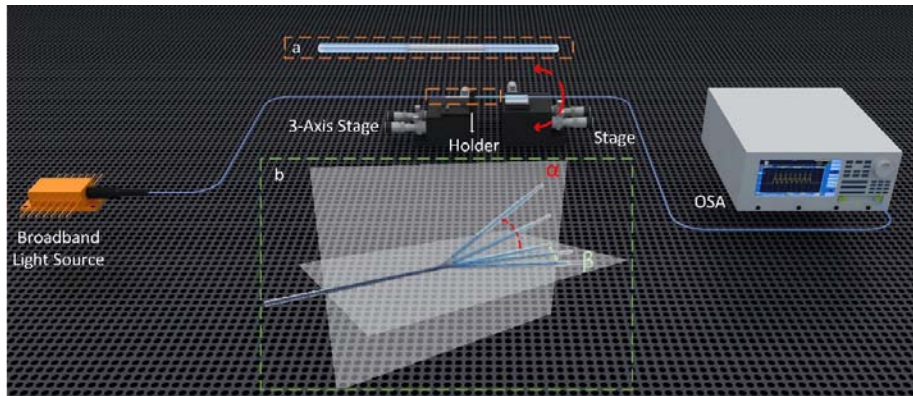
**Fig. 5.** Schematic diagram of the experimental setup; (Inset a) schematic structure of the bending sensor; (Inset b) schematic illustration of the bending angle measurement.

performance of this bending sensor. This property is inherent to the circular symmetry of the $HE_{11}$ and $HE_{12}$ modes.
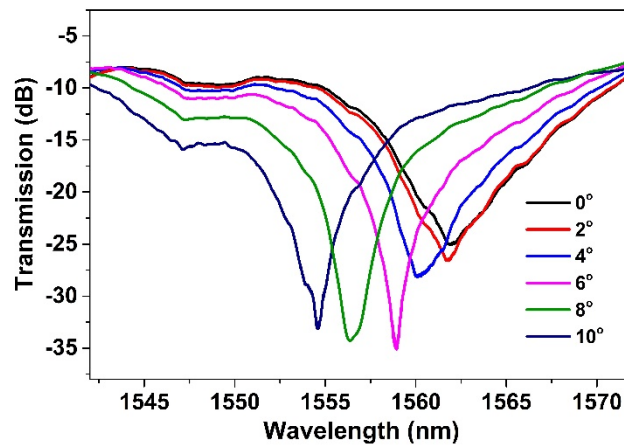


**Fig. 6.** Spectral evolution with bending angle increasing from 0° to 10° at horizontal plane.

The positions of the dip wavelength have been fitted with a two-orders polynomial fit (Fig. 7(a)). It is worth noticing that both curves (for vertical and horizontal planes) are well superposed. Furthermore, the good agreement of the polynomial fit indicates that the shift of the dip wavelength follows a two-order polynomial evolution with the bending angle. The bending sensitivity of the wavelength dip in orthogonal planes is then obtained from the derivative of these curves (Fig. 7(b)), leading to linear curves with a directional coefficient of 0.204. The sensitivity of our bending sensor is around 0.8 nm/deg for a bending angle of ± 4°, and up to 2.8 nm/deg for a bending angle of ± 14°. This sensitivity is about 10 times higher than the one reported by Liu *et al.* in this range of bending angle [24].

The reversibility of the sensor was also investigated by varying the bending angle from 0° to + 14° and back to 0°. The positions of the dip wavelength are plotted in the Fig. 7(c). They are almost identical in both cases (when the bending angle increases or decreases), which demonstrates the reversibility of our sensor. The shifting trend of the dip wavelengths versus bending angles (Fig. 7(a) and Fig. 7(c)) matches well with the simulated curve shown in Fig. 3(d).
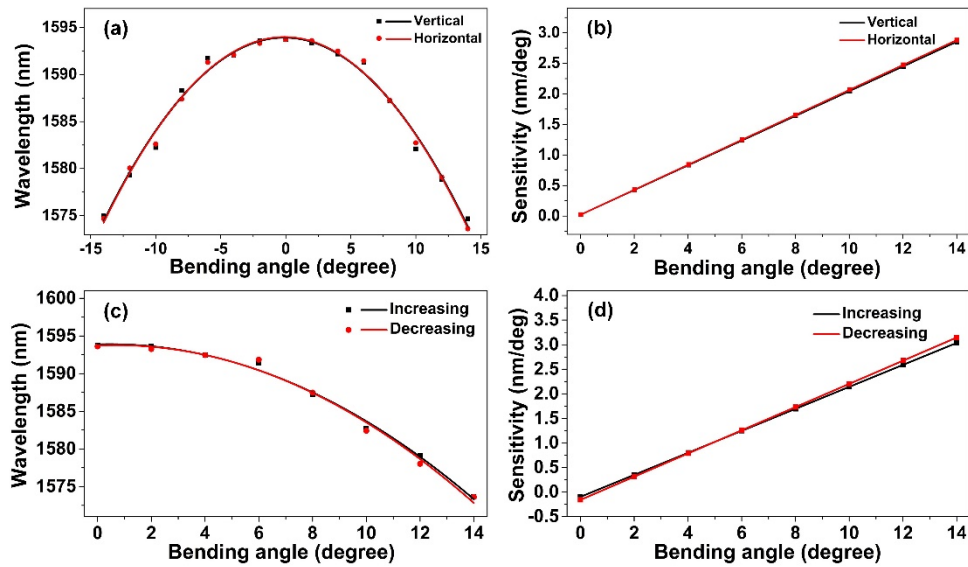
**Fig. 7.** (a) Bending angle response at two orthogonal planes; (b) linear sensitivity variations from 0° to 14° at two orthogonal planes; (c) reversibility measurement of the bending sensor; (d) linear sensitivity variations for reversibility measurement.

The results indicate that the nonlinear variation of mode interference of this HC-PCF under different bending angles is inherent and the reliability of experimental results is demonstrated.

The thermal sensitivity of our fiber sensor was measured by inserting it into a furnace (MTI GSL-1500x). The fiber was kept straight with a tiny tension in the furnace. The temperature of the furnace was increased from 18 °C to 1000 °C. The temperature precision of this furnace was 1 °C. The shift of the transmission spectrum was recorded with the broadband source and the OSA. The spectrum slightly shifts to longer wavelength with the temperature, as illustrated in Fig. 8(a) by the evolution of two wavelength dips. Both wavelength dips follow a linear shift with a directional coefficient of about 2.5 pm/°C. From these measurements, we can calculate a temperature cross-sensitivity of 0.0031 deg/°C and 0.0009 deg/°C for a bending angle of ± 4°
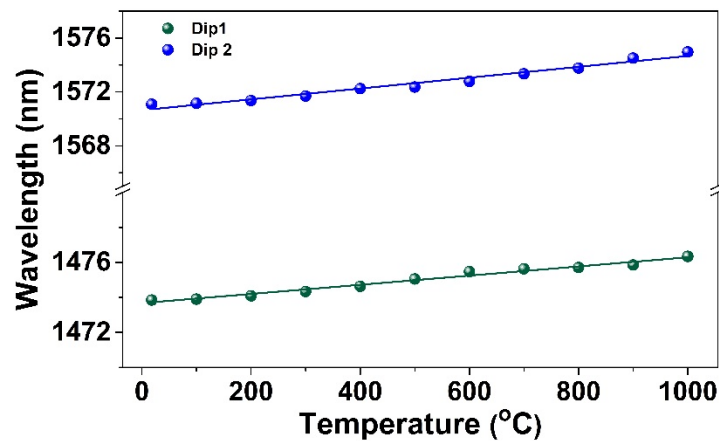


**Fig. 8.** Thermal responses of dip 1 (blue) and dip 2 (green) with a 5.0 cm length HC-PCF.

and ± 14°, respectively. The low temperature cross-sensitivity confirms the advantage of this HC-PCF for developing bending sensors. Furthermore, the weak degradation of the transmission spectrum at 1000°C (plotted in Fig. 8(b)) demonstrates the capability of our fiber sensor to measure small bending angles in a high temperature environment.

## 4. Conclusion

In summary, we investigate the bending measurement based on a specially designed HC-PCF with a large hollow core and small cladding. This fiber design enables the fiber diameter around 125 μm for easier bending and integration in fiber sensor configurations. Numerical simulation reveals that the bending sensitivity is mainly determined by the diameter of the hollow core and also depends on the coupled modes. Experimentally, the sensing device is fabricated by sandwiching the HC-PCF between two segments of SMFs. Compared with the [24], the bending sensitivity (2.8 nm/deg at 14°) is improved 10 times without orientation dependency by enlarging the mode field of the HC-PCF. Furthermore, based on the simulation results, the bending sensitivity can be improved by coupling $HE_{11}$ mode to $TE_{01}$ mode in our HC-PCF with offset splicing, but at the expense of a low robustness. Additionally, the low thermal sensitivity of 2.5 pm/°C from 18 °C to 1000 °C is also validated, which addresses the critical issue of thermal crosstalk for the highly sensitive bending measurement. Our research results unveil the performance optimization of the HC-PCF bending sensors, as well as extend the framework of microstructured fiber based sensing applications.

## References

1. J. Wang, F. Ai, Q. Sun, T. Liu, H. Li, Z. Yan, and D. Liu, "Diaphragm-based optical fiber sensor array for multipoint acoustic detection," Opt. Express **26**(19), 25293–25304 (2018).
2. N. M. Y. Zhang, K. Li, T. Zhang, P. Shum, Z. Wang, Z. Wang, N. Zhang, J. Zhang, T. Wu, and L. Wei, "Electron-rich two-dimensional molybdenum trioxides for highly integrated plasmonic biosensing," Sens. Actuators, B **5**(2), 347–352 (2018).
3. K. Li, N. Zhang, N. M. Y. Zhang, G. Liu, T. Zhang, and L. Wei, "Ultrasensitive measurement of gas refractive index using an optical nanofiber coupler," Opt. Lett. **43**(4), 679–682 (2018).
4. N. Zhang, G. Humbert, T. Gong, P. P. Shum, K. Li, J.-L. Auguste, Z. Wu, D. J. J. Hu, F. Luan, Q. X. Dinh, M. Olivo, and L. Wei, "Side-channel photonic crystal fiber for surface enhanced Raman scattering sensing," Sens. Actuators, B **223**, 195–201 (2016).
5. B. Shuai, L. Xia, and D. Liu, "Coexistence of positive and negative refractive index sensitivity in the liquid-core photonic crystal fiber based plasmonic sensor," Opt. Express **20**(23), 25858–25866 (2012).
6. Y. Zheng, Z. Wu, P. Ping Shum, Z. Xu, G. Keiser, G. Humbert, H. Zhang, S. Zeng, and X. Quyen Dinh, "Sensing and lasing applications of whispering gallery mode microresonators," Opto-Electron. Adv. **1**(9), 18001501–18001510 (2018).
7. G. Kim, T. Cho, K. Hwang, K. Lee, K. S. Lee, Y.-G. Han, and S. B. Lee, "Strain and temperature sensitivities of an elliptical hollow-core photonic bandgap fiber based on Sagnac interferometer," Opt. Express **17**(4), 2481–2486 (2009).
8. S. Zhang, W. Zhang, S. Gao, P. Geng, and X. Xue, "Fiber-optic bending vector sensor based on Mach–Zehnder interferometer exploiting lateral-offset and up-taper," Opt. Lett. **37**(21), 4480–4482 (2012).
9. W. Cui, J. Si, T. Chen, and X. Hou, "Compact bending sensor based on a fiber Bragg grating in an abrupt biconical taper," Opt. Express **23**(9), 11031–11036 (2015).
10. K. Ni, T. Li, L. Hu, W. Qian, Q. Zhang, and S. Jin, "Temperature-independent curvature sensor based on tapered photonic crystal fiber interferometer," Opt. Commun. **285**(24), 5148–5150 (2012).
11. Y. Wang, D. Richardson, G. Brambilla, X. Feng, M. Petrovich, M. Ding, and Z. Song, "Intensity measurement bend sensors based on periodically tapered soft glass fibers," Opt. Lett. **36**(4), 558–560 (2011).

12. L. C. Bobb, P. Shankar, and H. D. Krumboltz, "Bending effects in biconically tapered single-mode fibers," J. Lightwave Technol. **8**(7), 1084–1090 (1990).
13. S. Dass and R. Jha, "Microfiber-Wrapped Bi-Conical-Tapered SMF for Curvature Sensing," IEEE Sens. J. **16**(10), 3649–3652 (2016).
14. J. N. Dash, S. Dass, and R. Jha, "Photonic crystal fiber microcavity based bend and temperature sensor using micro fiber," Sens. Actuators, A **244**, 24–29 (2016).
15. G. Flockhart, W. MacPherson, J. Barton, J. Jones, L. Zhang, and I. Bennion, "Two-axis bend measurement with Bragg gratings in multicore optical fiber," Opt. Lett. **28**(6), 387–389 (2003).
16. W. MacPherson, M. Gander, R. McBride, J. Jones, P. Blanchard, J. Burnett, A. Greenaway, B. Mangan, T. Birks, and J. Knight, "Remotely addressed optical fibre curvature sensor using multicore photonic crystal fibre," Opt. Commun. **193**(1-6), 97–104 (2001).
17. J. P. Moore and M. D. Rogge, "Shape sensing using multi-core fiber optic cable and parametric curve solutions," Opt. Express **20**(3), 2967–2973 (2012).
18. P. Saffari, T. Allsop, A. Adebayo, D. Webb, R. Haynes, and M. M. Roth, "Long period grating in multicore optical fiber: an ultra-sensitive vector bending sensor for low curvatures," Opt. Lett. **39**(12), 3508–3511 (2014).
19. J. Kong, X. Ouyang, A. Zhou, H. Yu, and L. Yuan, "Pure Directional Bending Measurement With a Fiber Bragg Grating at the Connection Joint of Eccentric-Core and Single-Mode Fibers," J. Lightwave Technol. **34**(14), 3288–3292 (2016).
20. J. Kong, A. Zhou, C. Cheng, J. Yang, and L. Yuan, "Two-Axis Bending Sensor Based on Cascaded Eccentric Core Fiber Bragg Gratings," IEEE Photonics Technol. Lett. **28**(11), 1237–1240 (2016).
21. H. J. Patrick, "Self-aligning bipolar bend transducer based on long period grating written in eccentric core fibre," Electron. Lett. **36**(21), 1763–1764 (2000).
22. X. Chen, C. Zhang, D. J. Webb, K. Kalli, and G.-D. Peng, "Highly Sensitive Bend Sensor Based on Bragg Grating in Eccentric Core Polymer Fiber," IEEE Photonics Technol. Lett. **22**(11), 850–852 (2010).
23. X. Chen, C. Zhang, D. J. Webb, G. D. Peng, and K. Kalli, "Bragg grating in a polymer optical fibre for strain, bend and temperature sensing," Meas. Sci. Technol. **21**(9), 094005 (2010).
24. S. Liu, N. Liu, M. Hou, J. Guo, Z. Li, and P. Lu, "Direction-independent fiber inclinometer based on simplified hollow core photonic crystal fiber," Opt. Lett. **38**(4), 449–451 (2013).
25. J. Villatoro, V. P. Minkovich, and J. Zubia, "Photonic crystal fiber interferometric vector bending sensor," Opt. Lett. **40**(13), 3113–3116 (2015).
26. H. Zhang, Z. Wu, P. P. Shum, R. Wang, X. Q. Dinh, S. Fu, W. Tong, and M. Tang, "Fiber Bragg gratings in heterogeneous multicore fiber for directional bending sensing," J. Opt. **18**(8), 085705 (2016).
27. A. Grillet, D. Kinet, J. Witt, M. Schukar, K. Krebber, F. Pirotte, and A. Depre, "Optical Fiber Sensors Embedded Into Medical Textiles for Healthcare Monitoring," IEEE Sens. J. **8**(7), 1215–1222 (2008).
28. C. Zhan, Y. Zhu, S. Yin, and P. Ruffin, "Multi-parameter harsh environment sensing using asymmetric Bragg gratings inscribed by IR femtosecond irradiation," Opt. Fiber Technol. **13**(2), 98–107 (2007).
29. R. T. Schermer and J. H. Cole, "Improved Bend Loss Formula Verified for Optical Fiber by Simulation and Experiment," IEEE J. Quantum Electron. **43**(10), 899–909 (2007).
30. J. Su, X. Dong, and C. Lu, "Characteristics of Few Mode Fiber Under Bending," IEEE J. Sel. Top. Quantum Electron. **22**(2), 139–145 (2016).
31. M. H. Frosz, P. Roth, M. C. Günendi, and P. S. J. Russell, "Analytical formulation for the bend loss in single-ring hollow-core photonic crystal fibers," Photonics Res. **5**(2), 88–91 (2017).